

See discussions, stats, and author profiles for this publication at: <https://www.researchgate.net/publication/267853090>

Four dimensional hybrid ultrasound and optoacoustic imaging via passive element optical excitation in a hand-held probe

ARTICLE *in* APPLIED PHYSICS LETTERS · OCTOBER 2014

Impact Factor: 3.3 · DOI: 10.1063/1.4900520

CITATIONS

8

READS

87

3 AUTHORS, INCLUDING:



[Thomas Felix Fehm](#)

Technische Universität München

14 PUBLICATIONS 20 CITATIONS

[SEE PROFILE](#)



[Daniel Razansky](#)

Technical University of Munich and Helmholtz...

227 PUBLICATIONS 3,063 CITATIONS

[SEE PROFILE](#)

Four dimensional hybrid ultrasound and optoacoustic imaging via passive element optical excitation in a hand-held probe

Thomas Felix Fehm,^{1,2} Xosé Luís Deán-Ben,¹ and Daniel Razansky^{1,2,a)}

¹Institute for Biological and Medical Imaging (IBMI), Helmholtz Zentrum München, Neuherberg, Germany

²Faculty of Medicine, Technische Universität München, Munich, Germany

(Received 20 August 2014; accepted 9 October 2014; published online 28 October 2014)

Ultrasonography and optoacoustic imaging share powerful advantages related to the natural aptitude for real-time image rendering with high resolution, the hand-held operation, and lack of ionizing radiation. The two methods also possess very different yet highly complementary advantages of the mechanical and optical contrast in living tissues. Nonetheless, efficient integration of these modalities remains challenging owing to the fundamental differences in the underlying physical contrast, optimal signal acquisition, and image reconstruction approaches. We report on a method for hybrid acquisition and reconstruction of three-dimensional pulse-echo ultrasound and optoacoustic images in real time based on passive ultrasound generation with an optical absorber, thus avoiding the hardware complexity of active ultrasound generation. In this way, complete hybrid datasets are generated with a single laser interrogation pulse, resulting in simultaneous rendering of ultrasound and optoacoustic images at an unprecedented rate of 10 volumetric frames per second. Performance is subsequently showcased in phantom experiments and *in-vivo* measurements from a healthy human volunteer, confirming general clinical applicability of the method. © 2014 AIP Publishing LLC. [<http://dx.doi.org/10.1063/1.4900520>]

Pulse-echo ultrasound (US) is arguably the predominant imaging tool employed in modern clinical diagnostics, from obstetrics and gynecology to cancer staging, intravascular, and cardiac diagnostics.^{1–3} Combination of key advantages, such as real-time operation, safe use, portability and affordability, represents the unique signature of ultrasonography among the pantheon of medical imaging technologies. Yet, being based on mechanical properties of tissues, US mainly manifests structural information, generally limiting its specificity and diagnostic value.⁴ Integration of US with optoacoustic (OA) imaging may therefore significantly enhance the potential range of applications by bringing the optical contrast advantages of the optoacoustic modality, among them spectral specificity,^{5,6} functional hemodynamic contrast⁷ and powerful selection of highly efficient targeted,^{8,9} and activatable¹⁰ and genetically-encoded¹¹ contrast enhancement approaches. Several two-dimensional (cross-sectional) imaging approaches have been previously explored for combining OA with US. The most common one exploits the traditional US linear arrays by adding fiber-guided light irradiation on one or both sides of the array.¹² In this way, pulse-echo ultrasound and optoacoustic responses are recorded in an alternate order. An alternative approach consists in producing laser-induced US by illuminating a strong absorber positioned outside the object in the path of the excitation light.^{13,14} In this case, ultrasound transmission parameters (speed of sound and attenuation), not the usual pulse-echo contrast, can be extracted along with the optoacoustic absorption maps. However, as opposed to the relatively narrowband back-reflected US radiation, optoacoustically-generated signals usually possess an ultrawide bandwidth and manifold higher

tissue contrast. The application of acoustic focusing and common US beamforming or synthetic aperture approaches for OA image rendering is then generally challenging, leading to poor optoacoustic imaging performance for techniques based on these reconstruction approaches.¹⁵

Indeed, best imaging performance and image quantification in OA imaging and tomography implies the acquisition of three-dimensional tomographic information by means of unfocused detection of OA-induced responses from as many positions around the object as possible. In response, volumetric matrix array imaging probes with large number of detection elements densely distributed over spherical surface have been recently introduced.¹⁶ In contrast to the two-dimensional imaging approaches, this readily enabled real-time acquisition and rendering of volumetric OA images. Furthermore, by means of fast laser wavelength tuning, the unique capacities of five-dimensional OA imaging, i.e., real-time acquisition and unmixing of volumetric multi-spectral optoacoustic images, have been also showcased.⁶ In this letter, we introduce a concept for combined three-dimensional ultrasound and optoacoustic imaging with an acoustic beam excited via transient absorption of the excitation light. The optoacoustically-induced signals from the imaged tissues are then simultaneously recorded with the later arriving back-scattered ultrasonic waves by means of the spherical matrix array transducer. In this way, we are able to reproduce three-dimensional optoacoustic and pulse-echo ultrasound images in real time.

The proposed hand-held implementation for hybrid optoacoustic and ultrasound imaging is depicted in Fig. 1(a). The ultrasound beam is excited by light absorption at a passive element (PE) comprising a highly absorbing carbon microsphere with an approximate diameter of 400 μm (SPI-Supplies) located between the sample and the detection

^{a)}dr@tum.de

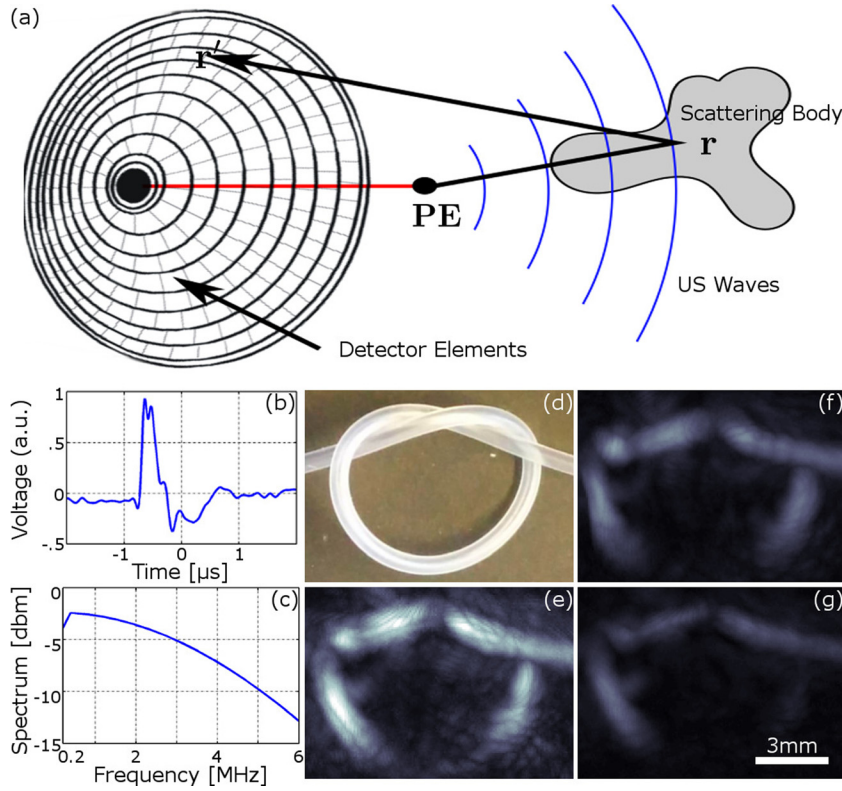


FIG. 1. Lay-out of the experimental setup. A $400\ \mu\text{m}$ diameter carbon microsphere is coaxially placed with respect to the optoacoustic excitation beam between the object and the spherical detector array. Optoacoustically-induced ultrasound waves emitted from the passive element (PE) carbon sphere are subsequently scattered inside the object at positions r before reaching the detector elements at positions r' . (b) and (c) Temporal profile and power spectrum density of the pressure waves emitted by the PE absorber. (d) Photograph of the tubing phantom. (e), (f), and (g) show the relative ultrasound scattering contrast achieved from three different substances: air, microbubble solution, and liquid ink, respectively. The color bar corresponds to ultrasound signal strength on an arbitrary scale.

array. Detection of back-scattered ultrasound is performed with a spherically-shaped array consisting of 256 piezocomposite elements (Imasonic SaS, Voray, France), as described in detail elsewhere.¹⁷ The individual detection elements have a size of $3 \times 3\ \text{mm}^2$, a central frequency of 4 MHz, and a $-6\ \text{dB}$ bandwidth of 100%. A central cavity is included in the array to enable coaxial optical excitation. The passive absorbing element was embedded in agar and placed along the central axis of the array, approximately 1.5 cm from the focal point in order to guarantee efficient illumination. The nanosecond-duration light pulses for optoacoustic excitation are generated by a tunable optical parametric oscillator (wavelength range 690–900 nm) laser source (SpitLight, Innolas Laser GmbH, Krailling, Germany) at a pulse repetition frequency (PRF) of 10 Hz. The beam is guided through a custom-made fiber bundle (CeramOptec GmbH, Bonn, Germany) that provides a Gaussian illumination profile at the tissue surface with a full-width at half maximum (FWHM) of approximately 10 mm. The time-resolved pressure signals at the 256 locations are simultaneously digitized by a custom-made high-speed data acquisition system (Falkenstein Mikrosysteme GmbH, Taufkirchen, Germany) triggered with the Q-switch output of the laser. The position of the carbon microsphere allows separating the optoacoustic waves generated within the tissue and the echoes from the passive-element ultrasound beam by simple time-windowing of the collected signals.

For the three-dimensional optoacoustic image reconstruction, we implemented a back-projection formula¹⁸ on a graphics processing unit (GPU), where the optoacoustic amplitude in arbitrary units at a given pixel $H(r'_j)$ is calculated via

$$H(r'_j) = \sum_i p_f(r_i, t_{ij}) - t_{ij} \partial_t p_f(r_i, t_{ij}), \quad (1)$$

being r_i the position of the i -th transducer element and $t_{ij} = |r'_j - r_i|/c$ the time-of-flight between r'_j and r_i , further assuming a constant speed of sound c in the medium. $p_f(r_i, t_{ij})$ represents the optoacoustically-induced spatio-temporal pressure distribution, obtained by measuring the signals around the object. For accurate signal recovery and optimal noise rejection, a filter combining deconvolution with the impulse response of the elements, differentiation, and a band-pass filter with cut-off frequencies of 0.75 and 7 MHz was applied to all the recorded signals in the time domain.

A similar reconstruction framework can, in principle, be considered for recovering the distribution of acoustic scatterers within the imaged tissue.¹⁹ However, several issues must be considered. On the one hand, the frequency spectrum of the signal emitted from the PE depends on its size, density, the longitudinal and transversal speed of sound.²⁰ The temporal profile of the optoacoustic signal emitted by the particular PE used in this study was measured using a calibrated broadband hydrophone (Precision Acoustics Ltd., Dorset, UK) and is shown in Fig. 1(b) along with its spectrum as calculated with the Welch spectral estimator (Fig. 1(c)). The signal of the PE was low-pass filtered at 6 MHz to remove high frequency noise. Clearly, the emitted spectrum is significantly broader than the effective detection bandwidth of the transducer elements. On the other hand, the directivity and frequency spectra of the back-scattered pressure waves are further affected by the type of scattering event. For instance, Rayleigh scattering would yield an isotropic far-field pattern and a frequency dependence of the scattering cross-section given by $1/\lambda^4$, where λ is the acoustic wavelength.²¹ Under a common assumption of single scattering events in soft biological tissues (weak scattering), the spatial distribution of scatterers can be subsequently reconstructed by means of a back-projection approach similar to the optoacoustic case.

Specifically, the ultrasound image at a certain voxel $U(r'_j)$ is estimated as

$$U(r'_j) = \sum_i s(r_i, t_{hij}), \quad (2)$$

being $t_{hij} = |r_h - r'_j|/c + |r'_j - r_i|/c$ the total time of flight from the location of the passive element r_h to the location of the acoustic scatterer r'_j and from there to the location of the detector r_i . In fact, Eq. (2) closely resembles traditional delay-and-sum ultrasound beamforming²² but with the function $s(r_i, t_{hij})$ back-projected along ellipses whose foci are the passive element and the location of each transducer. Note that $s(r_i, t_{hij})$ may instead account for the exact forward model of broadband sound propagation and directional scattering in heterogeneous tissues; however, theoretical derivation is challenging in this case. Nevertheless, in deriving an efficient implementation of reflection-mode ultrasound imaging using optoacoustically-induced radiation in the PE, $s(r_i, t_{hij})$ in Eq. (2) was taken as the filtered pressure $p_f(r_i, t_{ij})$, whereas a band-pass filter was applied (cut-off frequencies set between 2 MHz and 4 MHz) in order to optimize resolution and contrast of the images. In this way, the lower frequency boundary of the detected spectrum is responsible for establishing the diffraction-limited spatial resolution in the US imaging mode. Similarly to the conventional pulse-echo ultrasonography,²³ it is assumed here that the size of acoustic scatterers in the imaged tissue is much smaller than the wavelength of the detected waves.

Visualization in both optoacoustic and ultrasound modes relies on a GeForce GTX 780 implementation of the reconstruction algorithms using CUDA, which is capable of on-the-fly image rendering at a higher speed than the inter-pulse duration (1/PRF) of the laser. For a three-dimensional grid consisting of $128 \times 128 \times 96$ voxels, reconstruction rates of at least 100 volumes per second can be achieved.

Validation of the suggested hybrid approach was first performed in phantom experiments. A polyethylene tube with an inner diameter of 0.6 mm was tangled in a knot as displayed in Fig. 1(d). The knot was positioned around the center of the spherical ultrasound array, thus ensuring maximum sensitivity of all elements. The wavelength of the laser was set to 750 nm. Injection of different scattering and absorbing substances into the tubing was performed by means of an automatic injection pump (Harvard Apparatus, Holliston, USA) using a volume rate of 0.028 ml/s (≈ 1 cm/s). Figs. 1(e)–1(g) present the relative back-scattering ultrasound contrast provided by the tubing when filled with air, suspension of a microbubble contrast agent (SonoVue, Bracco Group, Italy), and Black India ink solution (Higgins Ink, Sanford, USA), respectively. For real-time visualization of dynamic phenomena, two injection experiments were performed. In the first experiment, the tubing initially contained air, which was slowly replaced by the ink solution, having effective optical absorption coefficient of $\mu_a = 2.3 \text{ cm}^{-1}$. The injection rate was maintained constant until the phantom was completely filled with the ink solution. In the second experiment, the tube was initially filled with the ink solution while the microbubble contrast agent (SonoVue, Bracco Group, Italy) was subsequently injected for contrast enhancement. Results of the

imaging experiments are presented in Fig. 2, clearly evincing that the spatial distribution dynamics of both light absorption and acoustic scattering can be simultaneously imaged in real time. Three representative time instants are shown in Fig. 2 for the two imaging experiments; however, the entire time sequence of the images is available in the online version of the journal. While air and ink only provide strong contrast in either ultrasound or optoacoustic images, the microbubble solution generates significant contrast for both modalities. To this end, microbubble contrast agents have significantly enhanced the imaging capacities in medical ultrasound diagnosis, drug and gene delivery applications.²⁴ Here, it was found that the common ultrasound contrast agent also provides detectable contrast for optoacoustic imaging at clinically applied concentration. The shape of the knot can be clearly distinguished in all images while the interface between the substances inside the tubing can be further tracked in real time, as shown, e.g., in Fig. 2(a) for $t = 0.7$ s (labelled with a white arrow). An additional example of well-registered OA

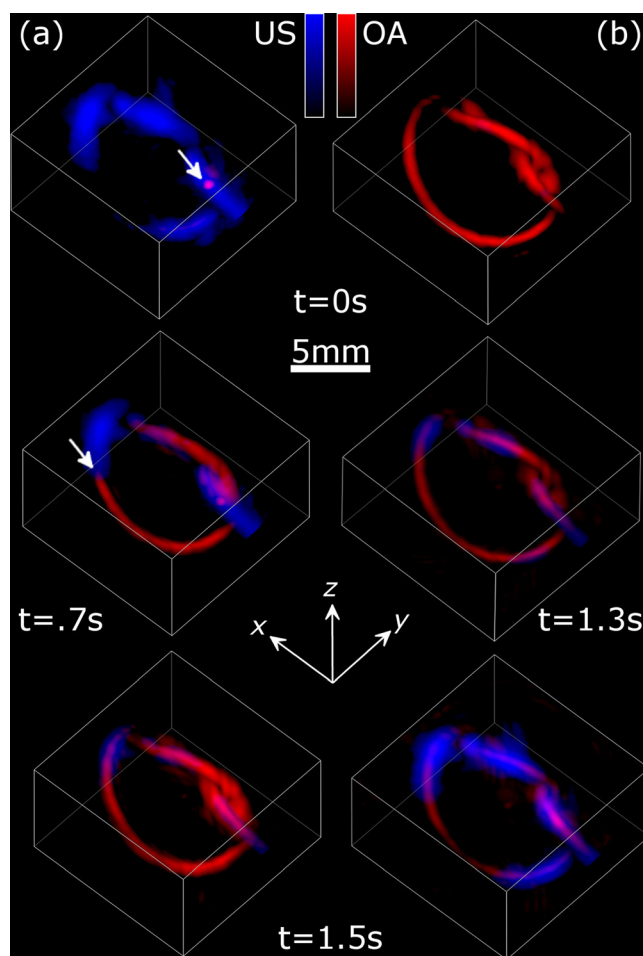


FIG. 2. Three-dimensional hybrid visualizations of fast contrast variations at video rate. (a) The reconstructed optoacoustic (red color scheme) and ultrasound (blue color scheme) images represent the experiment corresponding to the tubing phantom filled with air before an ink solution ($\mu_a = 2.3 \text{ cm}^{-1}$) is injected at $t = 0$ s. Details like an ink droplet leftover from a previous experiment and the boundary between air and the ink solution when the tubing is partially filled are indicated by white arrows. (b) Results from the second experiment where the phantom is initially filled with the ink solution before the microbubble contrast agent is injected. The maximum ultrasound signal strength provided by the microbubbles is achieved at $t = 1.5$ s. (Multimedia View) [URL: <http://dx.doi.org/10.1063/1.4900520.1>] [URL: <http://dx.doi.org/10.1063/1.4900520.2>]

and US images can be seen in Fig. 2(a) for $t = 0$ s, where an ink droplet leftover from a previous experiment (labelled with a white arrow) can be clearly identified inside the tubing. On the other hand, the onset of the ultrasound signal in Fig. 2(b) is delayed and reaches its full strength when the tubing is completely filled with the ultrasound contrast agent. The maximum value of the ultrasound image in Fig. 2(b) at $t = 1.5$ s was found to be approximately two thirds of the air filled phantom in Fig. 2(a) at $t = 0$ s.

A second set of experiments was carried out in order to provide an estimate of the lateral resolution and size of the field of view for the back-scattering ultrasound mode. A glass microsphere with an approximate diameter of $500\ \mu\text{m}$ (Cospheric, Santa Barbara, USA) was positioned in the vertical plane corresponding to the center of the spherical probe. The reflected signals were then recorded for different lateral positions of the sphere and the ultrasound images were reconstructed using Eq. (2). The resulting three-dimensional images as a function of the position of the microsphere are shown in a movie file available in the online version of the journal.²⁵ The size of the reconstructed glass microsphere for each individual image was defined as the FWHM. Analogously, the field of view was defined as the FWHM of the maximum pixel value as a function of the lateral position of the microsphere. This results in an estimated lateral size of the field of view of 10 mm. On the other hand, the size of the reconstructed sphere was approximately $500\ \mu\text{m}$ for all lateral positions, indicating that the spatial resolution in the pulse-echo ultrasound mode is substantially better than $500\ \mu\text{m}$. Clearly, the size of the reconstructed sphere is affected by the diameters of both the light absorber and the acoustic scatterer, so that a better estimate of the resolution is achieved when using smaller microspheres, which was, however, not accomplished in the current study due to rapid deterioration of the contrast to noise ratio for smaller scatterers. Nevertheless, it was previously shown that the resolution of the optoacoustic images, achieved by the spherical matrix array used in this study, was in the range $200\ \mu\text{m}$ at the geometrical center of the sphere,¹⁷ so that a similar resolution would also be expected for the ultrasound mode.

The performance of the hybrid probe in imaging of living biological tissues was showcased in a finger of a healthy volunteer. Human experiments were performed in full accordance with work safety regulations of Helmholtz Center Munich. A representative hybrid contrast image is displayed in Fig. 3. Clearly, while the ultrasound signals mainly manifest features related to the acoustic back-scattering at the surface of the skin and the bone (labeled on blue color scale in Fig. 3(a)), the optoacoustic data emphasizes a different type of optical absorption contrast arising from blood vessels located between the skin and the bone (labeled on red color scale). The additional structural contrast provided by superimposition of the US images may facilitate localization of the functional blood contrast visualized in the optoacoustic mode. Furthermore, the position of structures like the skin or the bone represent a valuable prior imaging information that can be subsequently employed to determine areas with a different speed of sound or regions where strong acoustic scattering takes place, thus help improve the optoacoustic reconstructions.^{26,27}

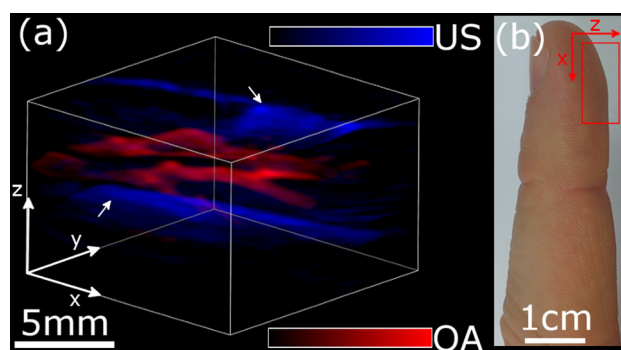


FIG. 3. Hybrid imaging of finger in a healthy volunteer. (a) Three dimensional views of the optoacoustic and ultrasound reconstructions are displayed in red and blue, respectively. The ultrasound image allows visualizing the location of the skin and the bone surface (labelled by white arrows) while optoacoustic signals mainly convey contrast of the blood vessels. The imaged region in the finger is shown in (b).

In summary, we have demonstrated simultaneous optoacoustic and ultrasound image acquisition at an unprecedented volumetric frame rate of 10 Hz. Temporal resolution of our method is established by the pulsed laser, therefore significantly better frame rate can be achieved by employing lasers with higher pulse repetition frequency. On the other hand, it is also important to notice that the conventional three-dimensional ultrasound, performed in the active send-receive mode, is severely limited in terms of its temporal resolution due to the large number of A-lines to be scanned.²⁸ Most recently, ultrafast ultrasound imaging approaches have been introduced, based on simultaneous detection of echoes produced by plane waves.²⁹ Despite significant acceleration of the achievable frame rates in both 2D and 3D, the latter approaches still require active generation of ultrasound waves, complicating their integration and synchronization with the optoacoustic imaging capability. Several limitations of the introduced approach require further attention. The three-dimensional matrix array probe, employed in the current study, is specifically optimized for optoacoustic tomographic imaging in a hand-held mode.¹⁷ However, its relatively low number of piezoelectric elements, their orientation, and the large pitch are not optimal for the delay-and-sum beamforming approach used in standard pulse-echo ultrasound imaging, which may result in significant grating lobe artifacts and loss of spatial resolution and contrast.²² A better hardware design, particularly pertaining the size, shape, and position of the passive element(s), is yet another crucial aspect for optimizing the signal-to-noise ratio and frequency content of the signals and, hence, maximize image contrast and resolution. Nevertheless, signal levels detected with the current design were sufficient to achieve proof of concept of real-time hybrid imaging in both phantoms and living human tissues.

D.R. acknowledges support from the European Union under Grant Agreement No. ERC-2010-StG-260991. The authors would like to acknowledge Professor Gil G. Westmeyer for providing the microbubble contrast agent.

¹P. W. Callen, *Ultrasonography in Obstetrics and Gynecology* (Elsevier Health Sciences, 2011).

²E. I. Bluth and C. B. Benson, *Ultrasonography in Vascular Diseases: A Practical Approach to Clinical Problems* (Thieme, 2011).

- ³M. Hayat, *Methods of Cancer Diagnosis, Therapy and Prognosis: Breast Carcinoma* (Springer, 2008), Vol. 1.
- ⁴G. Schmidt, *Differential Diagnosis in Ultrasound Imaging: A Teaching Atlas* (Thieme, 2011).
- ⁵L. V. Wang and S. Hu, "Photoacoustic tomography: in vivo imaging from organelles to organs," *Science* **335**, 1458–1462 (2012).
- ⁶X. L. Deán-Ben and D. Razansky, "Adding fifth dimension to optoacoustic imaging: volumetric time-resolved spectrally enriched tomography," *Light: Sci. Appl.* **3**, e137 (2014).
- ⁷J. Yao, J. Xia, K. I. Maslov, M. Nasirivanaki, V. Tsytarev, A. V. Demchenko, and L. V. Wang, "Noninvasive photoacoustic computed tomography of mouse brain metabolism *in vivo*," *Neuroimage* **64**, 257–266 (2013).
- ⁸V. Ntziachristos and D. Razansky, "Molecular imaging by means of multispectral optoacoustic tomography (MSOT)," *Chem. Rev.* **110**, 2783–2794 (2010).
- ⁹C. Kim, C. Favazza, and L. V. Wang, "In vivo photoacoustic tomography of chemicals: High-resolution functional and molecular optical imaging at new depths," *Chem. Rev.* **110**, 2756–2782 (2010).
- ¹⁰J. Levi, S. R. Kothapalli, T.-J. Ma, K. Hartman, B. T. Khuri-Yakub, and S. S. Gambhir, "Design, synthesis, and imaging of an activatable photoacoustic probe," *J. Am. Chem. Soc.* **132**, 11264–11269 (2010).
- ¹¹D. Razansky, M. Distel, C. Vinegoni, R. Ma, N. Perrimon, R. W. Köster, and V. Ntziachristos, "Multispectral opto-acoustic tomography of deep-seated fluorescent proteins *in vivo*," *Nat. Photonics* **3**, 412–417 (2009).
- ¹²J. J. Niederhauser, M. Jaeger, R. Lemor, P. Weber, and M. Frenz, "Combined ultrasound and optoacoustic system for real-time high-contrast vascular imaging *in vivo*," *IEEE Trans. Med. Imaging* **24**, 436–440 (2005).
- ¹³J. Jose, R. G. Willeminck, W. Steenbergen, C. H. Slump, T. G. van Leeuwen, and S. Manohar, "Speed-of-sound compensated photoacoustic tomography for accurate imaging," *Med. Phys.* **39**, 7262–7271 (2012).
- ¹⁴B.-Y. Hsieh, S.-L. Chen, T. Ling, L. J. Guo, and P.-C. Li, "All-optical scanhead for ultrasound and photoacoustic dual-modality imaging," *Opt. Express* **20**, 1588–1596 (2012).
- ¹⁵C. Kim, T. N. Erpelding, L. Jankovic, M. D. Pashley, and L. V. Wang, "Deeply penetrating in vivo photoacoustic imaging using a clinical ultrasound array system," *Biomed. Opt. Express* **1**, 278–284 (2010).
- ¹⁶X. L. Deán-Ben and D. Razansky, "Functional optoacoustic human angiography with handheld video rate three dimensional scanner," *Photoacoustics* **1**, 68–73 (2013).
- ¹⁷X. L. Deán-Ben and D. Razansky, "Portable spherical array probe for volumetric real-time optoacoustic imaging at centimeter-scale depths," *Opt. Express* **21**, 28062–28071 (2013).
- ¹⁸M. Xu and L. V. Wang, "Universal back-projection algorithm for photoacoustic computed tomography," *Phys. Rev. E* **71**, 016706 (2005).
- ¹⁹X. L. Deán-Ben, V. Ntziachristos, and D. Razansky, "Artefact reduction in optoacoustic tomographic imaging by estimating the distribution of acoustic scatterers," *J. Biomed. Opt.* **17**, 110504 (2012).
- ²⁰M. Khan and G. Diebold, "The photoacoustic effect generated by an isotropic solid sphere," *Ultrasonics* **33**, 265–269 (1995).
- ²¹J. J. Bowman, T. B. Senior, and P. L. Uslenghi, "Electromagnetic and acoustic scattering by simple shapes," Technical Report (DTIC Document, 1970).
- ²²K. E. Thomenius, "Evolution of Ultrasound Beamformers," in *IEEE Proceedings of the Ultrasonics Symposium* (IEEE, 1996), Vol. 2, pp. 1615–1622.
- ²³K. K. Shung and G. A. Thieme, *Ultrasonic Scattering in Biological Tissues* (CRC Press, 1992).
- ²⁴E. Stride and N. Saffari, "Microbubble ultrasound contrast agents: a review," *Proc. Inst. Mech. Eng. Part H* **217**, 429–447 (2003).
- ²⁵See supplementary material at <http://dx.doi.org/10.1063/1.4900520> for a movie showing the US image of the sphere at different lateral positions.
- ²⁶J. Jose, R. G. Willeminck, S. Resink, D. Piras, J. Van Hespén, C. H. Slump, W. Steenbergen, T. G. van Leeuwen, and S. Manohar, "Passive element enriched photoacoustic computed tomography (per pact) for simultaneous imaging of acoustic propagation properties and light absorption," *Opt. Express* **19**, 2093–2104 (2011).
- ²⁷X. L. Deán-Ben, V. Ntziachristos, and D. Razansky, "Acceleration of optoacoustic model-based reconstruction using angular image discretization," *IEEE Trans. Medical Imaging* **31**, 1154–1162 (2012).
- ²⁸A. Ng and J. Swanevelter, "Resolution in ultrasound imaging," *Contin. Educ. Anaesth. Crit. Care Pain* **11**, 186–192 (2011).
- ²⁹M. Tanter and M. Fink, "Ultrafast imaging in biomedical ultrasound," *IEEE Trans. Ultrason. Ferroelectr. Freq. Control* **61**, 102–119 (2014).